The diurnal behavior of evaporative fraction in the soil-vegetation-atmospheric boundary layer continuum

P. Gentine, D. Entekhabi, Jan Polcher

The Diurnal Behavior of Evaporative Fraction in the Soil–Vegetation–Atmospheric Boundary Layer Continuum

PIERRE GENTINE

Department of Applied Physics and Applied Mathematics, Columbia University, New York, New York

DARA ENTEKHABI

Department of Civil and Environmental Engineering, Massachusetts Institute of Technology, Cambridge, Massachusetts

JAN POLCHER

Laboratoire de Météorologie Dynamique, CNRS/IPSL, Paris, France

(Manuscript received 29 December 2009, in final form 24 March 2011)

ABSTRACT

The components of the land surface energy balance respond to periodic incoming radiation forcing with different amplitude and phase characteristics. Evaporative fraction (EF), the ratio of latent heat to available energy at the land surface, supposedly isolates surface control (soil moisture and vegetation) from radiation and turbulent factors. EF is thus supposed to be a diagnostic of the surface energy balance that is constant or self-preserved during daytime. If this holds, EF can be an effective way to estimate surface characteristics from temperature and energy flux measurements. Evidence for EF diurnal self-preservation is based on limited-duration field measurements. The daytime EF self-preservation using both long-term measurements and a model of the soil–vegetation–atmosphere continuum is reexamined here. It is demonstrated that EF is rarely constant and that its temporal power spectrum is wide; thus emphasizing the role of all diurnal frequencies associated with reduced predictability in its daylight response. Oppositely, surface turbulent heat fluxes are characterized by a strong response to the principal daily frequencies (daily and semi-daily) of the solar radiative forcing. It is shown that the phase lag and bias between the turbulent flux components of the surface energy balance are key to the shape of the daytime EF. Therefore, an understanding of the physical factors that affect the phase lag and bias in the response of the components of the surface energy balance to periodic radiative forcing is needed. A linearized model of the soil–vegetation–atmosphere continuum is used that can be solved in terms of harmonics to explore the physical factors that determine the phase characteristics. The dependency of these phase and offsets on environmental parameters—friction velocity, water availability, solar radiation intensity, relative humidity, and boundary layer entrainment—is then analyzed using the model that solves the dynamics of subsurface and atmospheric boundary layer temperatures and heat fluxes in a continuum. Additionally, the asymptotical diurnal lower limit of EF is derived as a function of these surface parameters and shown to be an important indicator of the self-preservation value when the conditions (also identified) for such behavior are present.

1. Introduction

Soil and vegetation control on evaporation results in adjustments in the components of the surface energy balance. The effects of these adjustments extend to the soil and atmosphere profiles of temperature, moisture, and heat fluxes. The changes in these profiles in turn affect the surface energy balance. Coupling of the soil and atmospheric boundary layer (ABL) profiles of temperature and heat fluxes can lead to the establishment of feedback mechanisms. The soil and ABL temperature profiles can reach states that would not be evident if these feedback mechanisms were not allowed to operate.

In this study, we focus on the partitioning of available energy at the surface into turbulent and ground heat

Corresponding author address: Pierre Gentine, Columbia University, 500 S.W. Mudd W. 120th St., New York, NY 10027.
E-mail: pg2328@columbia.edu

DOI: 10.1175/2011JHM1261.1

fluxes. The available energy has a strong diurnal cycle that principally follows the incident solar radiation. We are specifically concerned about the amplitude and phase of the surface energy balance components with respect to the principal forcing.

The evaporative fraction (EF) is a diagnostic of the surface energy balance that is supposedly unaffected by the strong periodicity in the forcing. Furthermore, it is supposed to isolate soil and vegetation control on evaporation from factors that have strong links to available energy and turbulence. If this is true, EF can be a very useful target of estimation using surface temperature measurements and energy balance modeling (Boni et al. 2001a,b; Caparrini et al. 2003, 2004a,b; Kustas et al. 2001; Margulis et al. 2002). It would isolate the soil and vegetation control from other factors in the determination of latent heat flux and other components of the surface energy balance. Evaporative fraction is defined as the fraction of available energy partitioned toward latent heat flux:

$$\mathrm{EF} = \frac{\lambda E}{A} = \frac{\lambda E}{H + \lambda E}. \tag{1}$$

The evaporative fraction is also related to the Bowen ratio B as

$$\mathrm{EF} = (1 + B)^{-1}. \tag{2}$$

Surface latent heat flux is governed by available energy (highly periodic), turbulence (highly variable but less periodic), and surface control (slowly varying). Surface control refers to root-zone soil moisture and water available to plants that vary on longer time scales than daytime. If EF truly isolates the surface control on turbulent heat fluxes and is nearly constant during daytime, it has major implications for sampling and estimation.

Several studies based on limited-duration field experiment observations (e.g., Shuttleworth et al. 1989; Nichols and Cuenca 1993; Crago 1996; Crago and Brutsaert 1996) show that EF could be considered to be a constant during daytime hours. This is referred to as the daytime self-preservation of EF. However, recent modeling studies by Lhomme and Elguero (1999) and Gentine et al. (2007) have shown that EF is nearly constant during daytime under limited environmental conditions. This study delves deeper into the underlying causes and degree of the apparent near self-preservation of EF during daytime.

The objective of the present study is to determine the factors controlling the shape of EF. Common fair-weather shapes of EF are gleaned using daily sinusoidal representation of the sensible heat flux and latent heat flux at the land surface. The typically observed shapes of EF are explained mostly by the phase and amplitude difference between sensible and latent heat fluxes.

The diagnostic EF is a ratio of two components of the surface energy balance that both have strong diurnal periodicities. We first use a simple mathematical example (turbulent fluxes as sinusoids) to show that the ratio diagnostic can easily take on a shape that is often observed and not characterized by daytime self-preservation if there is a phase lag or an offset among the turbulent fluxes. We therefore focus our attention on physical factors that cause phase lag and offsets between these two fluxes. To derive an expression for phase lag and amplitude gain of the turbulent fluxes that is in response to incoming radiation forcing and includes physical parameters, we need a model that represents the temperature and flux profiles in the soil–vegetation–atmosphere continuum in terms of harmonics. Harmonic decomposition (especially the phase response) of the soil–vegetation–atmosphere continuum requires a linear model of the continuum that captures the essential physics and linkages. There is a long history of using simpler and analytical models to gain insights into soil–ABL coupled systems (e.g., see Manqian and Jinjun 1993; Brubaker and Entekhabi 1994; Kimura and Shimizu 1994; Kim and Entekhabi 1998; Margulis and Entekhabi 1998; Zeng and Neelin 1999; Wang and Mysak 2000; Van de Wiel et al. 2002). In the present study, we use an extended version of the linear model of the soil–vegetation–ABL continuum introduced by Gentine et al. (2010) in order to analyze the phase and amplitude responses of sensible and latent heat fluxes at different temporal frequencies.

A distinct advantage of the analytical approach is that the phase and amplitude changes of surface turbulent heat fluxes can be studied as a function of environmental parameters (friction velocity, water availability, solar radiation intensity, relative humidity, and boundary layer entrainment). In this paper, we quantify the dependence of the critical phase lag and amplitude gain between the turbulent fluxes on physical factors in the environment. We show that EF is daytime self-preserved only under very limiting conditions: cloud-free, humid climate with intense solar radiation forcing. In other circumstances, EF is generally not self-preserved mainly because there is a difference in amplitude and phase between sensible and latent heat fluxes induced by their different response to radiative forcing. Even under these conditions, the critical midday value of EF is predictable based on environmental factors and measurements. We derived this limiting and useful value in this study.

2. Observational evidence

Several studies based on limited-duration field experiment observations have provided some evidence for occasional self preservation (i.e., constancy) of EF (e.g., Shuttleworth et al. 1989; Nichols and Cuenca 1993; Crago 1996; Crago and Brutsaert 1996). Short-duration studies do not allow the diagnosis of recurrent anomalous patterns in the EF diurnal cycle. In this study, we begin with the analysis of a long-term field experiment dataset that sets the stage for understanding the limits to the self-preservation assumption in the same location that are due to changes in the environmental conditions.

a. Dataset

The observational dataset corresponds to 101 (noncontinuous) days of measurements from the Sud Mediterannée (SUDMED) 2002 field campaign in Marrakech, Morocco as described in Duchemin et al. (2006), Gentine et al. (2007), and Chehbouni et al. (2008). The study site is a wheat field with relatively sparse vegetation [leaf area index (LAI) = 0.4 m^2 m^{-2} and vegetation height of 40 cm]. The R3 site is an irrigated 2800-ha area, located 45 km east of Marrakech. Two fields were equipped with instrumentation, namely the 123rd (R3-B123 used in this study) and 130th (R3-B130) parcels. The sowing date is 13 January (Julian day 13). The climate is characterized by a dry and warm period with very few precipitation events in the summer and fall. Almost all of the annual precipitation occurs in winter and spring. The rainy period lasts six months from November to April and the cumulative precipitation is generally of the order of 250 mm yr^{-1}. The site is periodically irrigated by flooding the entire field. The induced significant change in the energy partitioning at the land surface provides a useful experiment design for our study. The parcel of interest in this study is R3-B123. Irrigation events occurred on 4 February (day 35), 20 March (day 79), 13 April (day 103), and 21 April (day 111), with a mean supply of 25 mm each time.

Energy fluxes were continuously monitored, starting 4 February (day 35) and lasting the entire wheat season until 21 May (day 141). The measurements covered the entire phonological cycle: sowing, vegetative growth, full canopy, and senescence. Vegetation appears around 7 February (day 38), with a growth peak on 20 April (day 110), followed by the senescence period until the end of May. Near-continuous measurements have been recorded during the entire wheat season. Sensible heat flux was measured with a Campbell Scientific, Inc., 3D sonic anemometer (CSAT3) at 3-m height. A krypton hygrometer (KH_2O) measured the latent heat flux at this height. The net radiation is monitored by a Kipp and Zonen CNR1 radiometer located at 2 m above the ground. The air temperature was monitored at 6-m height using Vaisala temperature and humidity HMP45C probes, and the shortwave incoming radiation was recorded by at 1 m height with a Kipp and Zonen CM5 pyranometer.

The meteorological conditions are highly variable. Solar incoming radiation varies between a diurnal maximum of 200 W m^{-2} for a February cloudy day to a diurnal maximum between 900 and 1000 W m^{-2} at the end of May. There is also a wide range of air temperatures with a minimum of 0°C in February and a maximum of 38°C by the end of May.

b. Typical EF patterns

Two time series of evaporative fraction containing various solar conditions (fair, slightly, and highly cloudy) are depicted in Figs. 1 and 2 along with the corresponding solar radiation received at the land surface. These time series have been selected since they display typical courses of daylight EF in various conditions over a relatively short period. The time series show that daytime EF is rarely constant. Only in clear-sky conditions is the course of EF smooth with a typical convex shape (Lhomme and Elguero 1999; Gentine et al. 2007) as seen in Fig. 2. With light cloud cover (days 101, 102, and 106) EF displays a significant increase compared to adjacent days. Under intermittent-cloudy situations (days 104, 131, 134, 135, and 139), evaporative fraction exhibits strong spikes when solar radiation is attenuated by clouds. Its daytime pattern becomes erratic. Even under fair-weather conditions, EF is generally nonconstant during daytime and takes on a typical convex shape [day of year (DOY) 132, 133, 136, and 137]. To further investigate the global diurnal behavior and self-preservation of EF over the whole measurement period, we perform a spectral analysis that isolates the strength of variability (energy) in different time frequencies.

c. EF spectrum

The measurements of the SUDMED experiment are particularly suitable for a spectral analysis of EF. Indeed, only about 30 days out of the 101-day period of measurements contain clouds, and only 12 days present an attenuation of more than 20% of solar radiation for more than 3 h. These conditions are typical of semiarid climates, characterized by sparse clouds.

To investigate the EF spectrum and compare its shape to the spectra of its constituent surface heat fluxes, we introduce the daytime power spectrum for each variable. The spectra are normalized by the total spectral power (variance) in order to obtain dimensionless and comparable values. The daytime power spectrum is the average of the Fourier decomposition of the variable for

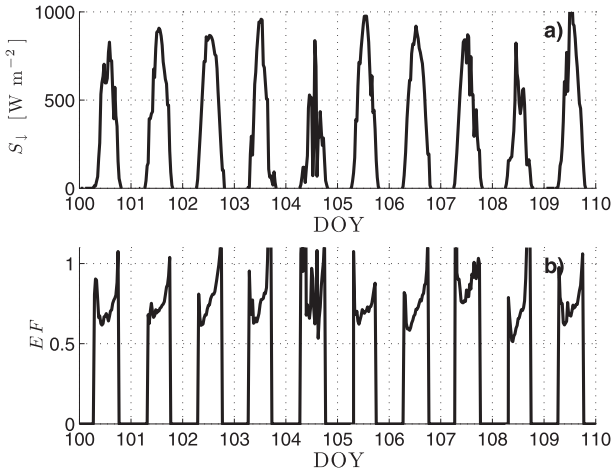

FIG. 1. Observed time series of (a) solar incoming radiation and (b) daytime EF after 10 days of the SUDMED field experiment (Julian days 100 to 110; LAI ranges from 3.0 to 3.5). The conditions are representative of scattered with few very cloudy conditions. EF exhibits a strong convexity with a sharp rise in the afternoon (inducing asymmetry in the daytime pattern). In very cloudy conditions (e.g., day 104), EF becomes erratic.

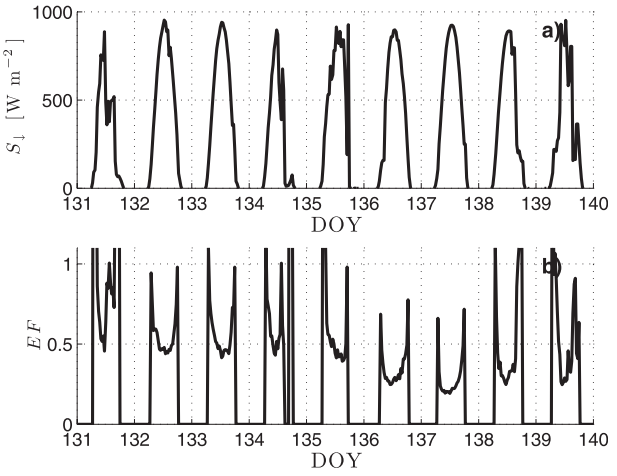

FIG. 2. Observed time series of (a) solar incoming radiation and (b) daylight EF during 9 days of the SUDMED field experiment project (Julian days 131 to 140; LAI ranges from 2.5 to 0.4 because of senescence). Days 132, 133, 136, and 137 represent generally cloud-free conditions that show a symmetric concave daytime EF pattern. During the remaining days, passing clouds lead to spikes in EF.

each day across 70 gap-free days. The full daily cycle is considered for the surface heat fluxes, whereas only daytime hours are used for EF.

The normalized power spectra of evaporative fraction, net radiation, and sensible and latent heat flux are depicted in Fig. 3. These power spectra show that most of the daytime spectral power of net radiation and turbulent heat fluxes are located at the diurnal and semidiurnal frequencies. Therefore, during most of the diurnal cycle, surface fluxes are explained by these low diurnal frequency harmonics. This is simply a consequence of the influence of the main solar radiation harmonic, which is composed of a daily and semidaily period. Nonetheless, this shape forms the reference for understanding the EF spectrum.

Evaporative fraction displays a broad power spectrum across all harmonics. This means that all diurnal frequencies have an impact on the EF diurnal response. The relative response of each harmonic is relatively weak (2% to 5%) and the average diurnal value of EF accounts for 72% of its total power spectrum, compared to 34% for net radiation, 35% for sensible heat flux, and 58% for latent heat flux. The construct of the EF diagnostic has reduced the importance of the characteristic diurnal and semidiurnal harmonics of solar radiation. This is conditional on where the sensible and latent heat fluxes respond in unison to solar radiative forcing (see next section). The widening of the spectrum of EF compared to that of turbulent heat fluxes is evident during cloudy conditions (Fig. 2). The important contribution of the high frequencies is more complicated to interpret.

Components of the surface energy balance that have significant periodicities have a natural Fourier representation:

$$A(t,z) = \overline{A}(z) + \sum_{\substack{n=-\infty \\ n\neq 0}}^{n=+\infty} \tilde{A}(n\omega_0, z) e^{jn\omega_0 t}, \qquad (3)$$

with A the surface heat flux and $\omega_0 = 2\pi/T$ the fundamental angular frequency. The tilde symbol represents the complex Fourier harmonic. Sensible and latent heat have strong periodicities owing to their direct dependence on the periodic radiation forcing. Evaporative fraction is thought to have less direct dependence on radiation forcing and, hence, may exhibit less pronounced periodicity.

Contrary to latent and sensible heat flux, there is no simple relationship between each harmonic of EF and their counterpart in the forcing of incident radiation (Gentine et al. 2010). Since EF is a fraction defined through (1) [i.e., $\mathrm{EF}(t) = \lambda E(t)/[H(t) + \lambda E(t)]$ or $\mathrm{EF}(t)[H(t) + \lambda E(t)] = \lambda E(t)$], its spectral solution involves a convolution in the frequency domain (tilde represents the Fourier amplitude—that is, harmonic at frequency ω):

$$\widetilde{\mathrm{EF}}(\omega) \times [\tilde{H}(\omega) + \widetilde{\lambda E}(\omega)] = \widetilde{\lambda E}(\omega), \qquad (4)$$

equivalent to

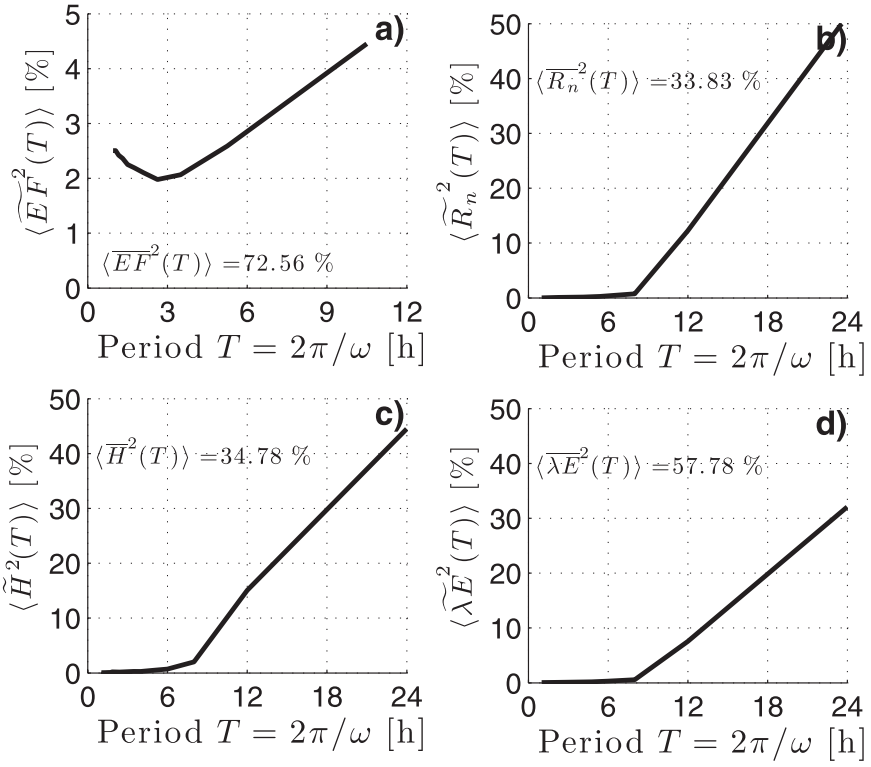

FIG. 3. Normalized power spectrum of the daily harmonics [i.e., ratio of the square amplitude of the harmonic $\langle \tilde{X}^2(T) \rangle$ relative to the total daily power spectrum $\sum_T \langle \tilde{X}^2(T) \rangle$] of (a) EF, (b) net radiation, (c) sensible heat flux, and (d) latent heat flux. The mean of the harmonic is calculated across the 101-day extensive period, except for days with missing measurement. Note that the surface heat fluxes are expressed on a 24-h basis, whereas EF is expressed only for daylight hours only (i.e., on a 12-h basis). The text in the figures indicates the relative contribution of the (a) mean-daytime $\overline{\mathrm{EF}}$ and mean-daily heat fluxes (b) $\overline{R_n}$, (c) $\overline{H}$, and (d) $\overline{\lambda E}$ to the total power spectrum.

$$\sum_{m=-\infty}^{+\infty} [\widetilde{H}[(n-m)\omega_0] + \widetilde{\lambda E}[(n-m)\omega_0]]\widetilde{\mathrm{EF}}(m\omega_0) = \widetilde{\lambda E}(n\omega_0). \quad (5)$$

Because of the convolution in the frequency domain, the spectrum of both sensible and latent heat flux impact and diffuse across the whole spectrum of EF. The power spectrum of EF is consequently much broader than that of sensible and latent heat flux, as observed on Fig. 3a. As a consequence, EF is generally nonpreserved during daylight hours and all diurnal harmonics are important components of its daylight response. This might lead to complications for the predictability of EF, characterized by important middle- to high-frequency components, whereas turbulent heat fluxes are mostly influenced by the daily and semidaily harmonic of the radiation forcing in fair-weather conditions. In addition, the wider spectra observed in the turbulent heat fluxes under cloudy and intermittent-cloudy conditions leads to broader distribution of power across frequencies for evaporative fraction because of the importance of all harmonics in the EF convolution in (4).

3. Factors affecting the shape of the EF diagnostic

Even under clear-sky conditions and in the absence of intermittent clouds, the diagnostic EF has a characteristic convex or U shape as shown in the SUDMED observations. Often the convexity is biased toward the late afternoon and there is asymmetry in the convexity. A sharp rise is evident in the afternoon.

Factors that can cause these anomalies in the daytime pattern of EF can become evident in a simple mathematical example of the ratio of two periodic signals. We identify these factors and then reproduce them in a model of the process physics. The physical factors that amplify such anomalies are identified in this way.

We examine the diurnal response of an evaporative fraction diagnostic when the turbulent heat fluxes are pure sinusoids. The sensible heat flux is

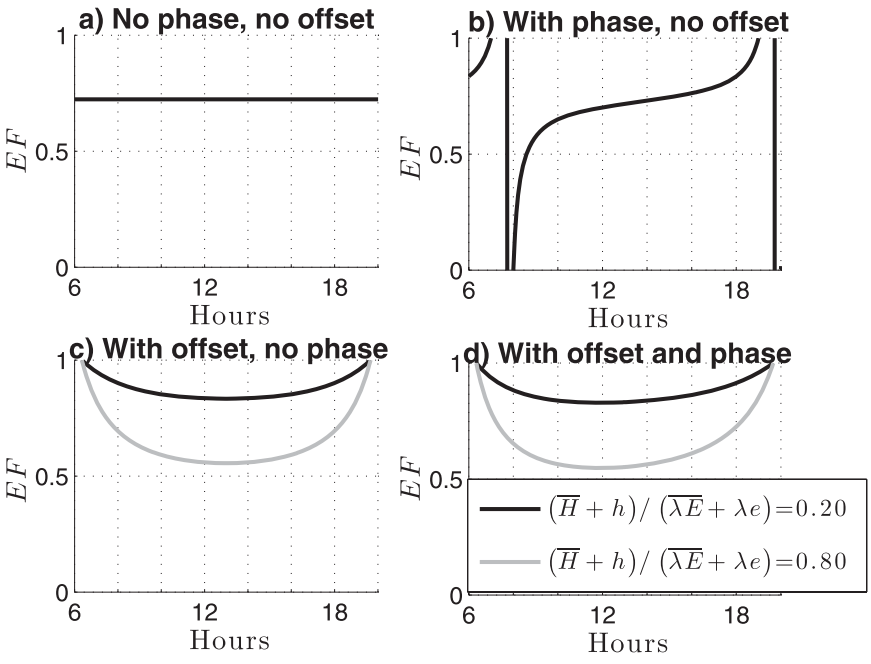

FIG. 4. Daytime patterns of EF resulting from a daily sinusoidal sensible heat flux $H(t) = \overline{H} + h\cos(\omega_0 t + \phi_H)$ and latent heat flux $\lambda E(t) = \overline{\lambda E} + \lambda e\cos(\omega_0 t + \phi_{\lambda E})$. (a),(c) The situation without phase difference $\phi_H = \phi_{\lambda E}$. (b),(d) The situation including a phase difference of 1 h between latent and sensible phase flux. (a) Both sensible and latent heat fluxes do not have a mean component and have the same phase. (b) The phase difference between both fluxes $\phi_H \neq \phi_{\lambda E}$ leads to strong departure from daytime EF self-preservation. We here use $\phi_{\lambda E} - \phi_H = 1$ h. (c) There is no phase difference between H and λE but they have nonzero mean value (value based on typical measurements). The daytime EF pattern exhibits the typical concave U shape as seen in observations. (d) Both the phase and the mean component are nonzero. Depending on the mean component, the shape can have either a U form or take the form of a tangent function.

$$H(t) = \overline{H} + h\cos(\omega_0 t + \phi_H), \tag{6}$$

and the latent heat flux is

$$\lambda E(t) = \overline{\lambda E} + \lambda e\cos(\omega_0 t + \phi_{\lambda E}), \tag{7}$$

with $\overline{H}$ and $\overline{\lambda E}$ representing mean-daily values, h and λe representing daily amplitudes, and ϕ_H and $\phi_{\lambda E}$ representing phase lags. The principal frequency ω_0 is diurnal.

Using trigonometric identities and introducing the phase difference between latent and sensible heat flux $\phi = \phi_{\lambda E} - \phi_H$, evaporative fraction can be rewritten

$$\mathrm{EF}(t) = \frac{1}{1 + \dfrac{\overline{H} + h}{\overline{\lambda E} + \lambda e[\cos(\phi) - \sin(\phi)\tan(\omega_0 t + \phi_H)]}}. \tag{8}$$

It is clear from this formula that the diurnal course of EF responds to several factors that include the relative amplitude and phase of the harmonic of turbulent heat fluxes. In addition, we expect a tangent-like shape of EF when $\omega_0 t + \phi_H \approx 0$ and $\phi = 0$ (i.e., around solar noon), as observed in Fig. 2. EF is constant only when there is no phase difference between sensible and latent heat flux (i.e., $\phi = 0$). In this case $\mathrm{EF}(t) = [1 + (\overline{H} + h)/(\overline{\lambda E} + \lambda e)]^{-1}$, which is composed of all constant terms. Consequently, EF in this simple example is constant only if the phase difference between sensible and latent heat flux is negligible.

The daytime reconstructions of EF are presented in Fig. 4a, which shows the self preservation of EF when sensible and latent heat fluxes are in phase, $\phi = 0$, and when there is no average daily component $\overline{H} = \overline{\lambda E} = 0$. Yet once a phase difference is introduced ($\phi \neq 0$), as shown in Fig. 4b, EF exhibits a tangent-like diurnal course, as observed in slightly cloudy situations in Fig. 1 (days 101, 102, and 106). The phase difference between sensible and latent heat flux is therefore an essential factor controlling the daytime pattern of EF. Figure 4c depicts the effect of nonzero average components of sensible and latent heat flux $\overline{H} \neq 0 \neq \overline{\lambda E}$ without phase difference $\phi = 0$. Two values of $(\overline{H} + h)/(\overline{\lambda E} + \lambda e)$ are

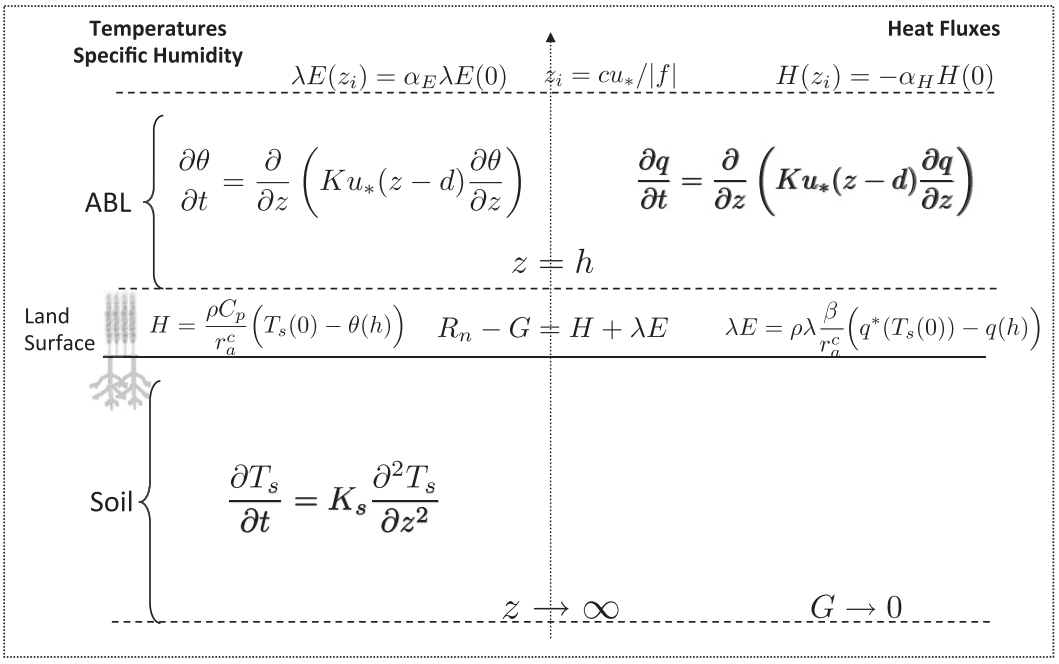

FIG. 5. Representation of the soil–vegetation–atmospheric boundary layer continuum for states and fluxes in the coupled land–atmosphere. The equations in black correspond to the original Lettau (1951) formulation. In this study, we added a discontinuity at the surface and the specific humidity state (equations in lighter gray) that are solved simultaneously. Whereas Lettau (1951) specified the value of latent heat flux, in this extension of the model, the latent heat flux is estimated based on gradients in humidity and temperature at the surface. Furthermore, the solution here covers all the harmonics contained within a day, whereas Lettau (1951) solved the system for only one harmonic.

presented in Fig. 4c in order to emphasize the importance of the amplitude of the turbulent heat fluxes for the daytime pattern of EF. The typical U shape of EF observed for field experiment clear-sky conditions is reconstructed with this simple model of the turbulent heat fluxes. The relative amplitude of the turbulent heat fluxes is essential to determine the minimum value of EF. Figure 4d represents the effect of both the nonzero phase and nonzero daily average sensible and latent heat fluxes. The response is relatively similar to the case of Fig. 4c, with a U shape, except that the phase difference yields an asymmetry in the daytime response of EF. This asymmetric pattern is often observed and it is evident in the SUDMED observations.

The daytime self-preservation and shape of EF is intimately linked to the phase difference between sensible and latent heat flux as well as to their relative amplitude. The physical factors affecting the phase difference between the two fluxes cannot be readily isolated and diagnosed using field observations. Many factors are varying at once and the isolation of key factors is not simple. Models that explicitly derive the phase and amplitude gains as a function of frequency need to be linear so that they can be directly solved in the Fourier domain. Here we use the land–atmosphere model introduced in Gentine et al. (2010) that meets the requirements. Even though this analytical model is simple and linear, Gentine et al. (2010) use comparisons with field experiment observations to show that the model adequately describes the intraday energy partitioning at the land surface. It responds to varying environmental conditions (wind speed, solar radiation, soil moisture, and vegetation cover) in a realistic fashion that is also evident in the field observations (see Gentine et al. 2010).

4. Amplitude and phase harmonic responses across the soil–vegetation–atmosphere continuum

a. Linear land–atmosphere model

A schematic representation of the land–atmosphere system is shown in Fig. 5. The model links the one-dimensional soil–vegetation–ABL continuum for the heat and moisture state variables and fluxes. In essence, the model used in this study is similar to the one introduced by Gentine et al. (2010) and inspired by the work of Lettau (1951). This model is used to analytically determine the response of the coupled land–atmosphere system to a daily periodic forcing of net radiation at the land surface. Even though the model relies on major

assumptions about some physical processes, it is shown to well reproduce the daily course of land surface heat fluxes and temperature, as well as the air temperature at screen level compared to measurements from the SUDMED project. The reader is referred to Gentine et al. (2010) for a complete description of the model construct and a list of the main assumptions. The most important assumptions are i) the atmospheric profile is in a near neutral-to-unstable turbulent state, ii) friction velocity is assumed to remain constant throughout the day, and iii) the ABL height is fixed. Since the factors affecting the partitioning of energy balance are mostly isolated in the surface layer (lower few meters of the ABL) and the near-surface soil, the assumptions about the profile stability and ABL-top height are not considered to be major factors that change the sensitivities that are isolated. The fidelity of the identified harmonic response of the energy partitioning in varying conditions is the important factor. Even though the time series of friction velocity are generally erratic, over the 70 days of SUDMED turbulent heat flux observations, 73% of the daily power spectrum of friction velocity is concentrated in the daily average and 93% of its daytime power spectrum is concentrated in the daytime average.

In Gentine et al. (2010), a constant EF was assumed. The model used in this study improves the model of Gentine et al. (2010) in several ways in order to study the phase difference between the turbulent heat fluxes:

i) Latent heat flux at the land surface is expressed using a bulk formulation (Deardorff 1978):

$$\lambda E(h) = \frac{\lambda \rho \beta}{r_a^c}[q^*(T_{s_0}) - q(h)]. \tag{9}$$

The parameter β reduces the evaporation below its limiting potential value corresponding to a moist surface. This parameter is related to the soil moisture in the root zone and it is assumed to be constant throughout the period T (one day). The main difficulty of the latent heat flux formulation is that the saturated-specific humidity is a nonlinear function of the temperature state. To the first-order approximation, this equation can be linearized around the mean land surface temperature over period T:

$$q^*(T_{s_0}) = q^*(\overline{T}_{s_0}) + (T_{s_0} - \overline{T}_{s_0})\left[\frac{dq^*(T)}{dT}\right]_{T=\overline{T}_{s_0}} = q^*(\overline{T}_{s_0}) + \gamma_{\overline{T}_{s_0}}(T_{s_0} - \overline{T}_{s_0}). \tag{10}$$

Introduction of dynamic latent heat flux term in the surface energy balance necessitates inclusion of a specific humidity variable in the ABL.

ii) A diffusion equation governing the evolution of specific humidity in the ABL is added and is similar to the diffusion equation of potential temperature presented in Gentine et al. (2010). The transport of this state uses the same diffusion coefficient as the temperature state. This equation has a Neuman boundary condition on top of the ABL and a jump condition at height h, which is given by the expression of latent heat at the land surface.

iii) In Gentine et al. (2010), the model was forced by the periodic net radiation at the land surface. Here we use the incoming radiation at the land surface, defined as the sum of net solar $S_\downarrow(1 - \alpha_s)$ and incoming thermal components $L_\downarrow$ as $I_\downarrow(t) = (1 - \alpha_s)S_\downarrow(t) + L_\downarrow(t)$. Net radiation is linearized around the mean land surface temperature over period T:

$$R_n(t) = \underbrace{(1 - \alpha_s)\overline{S} + \overline{L}_\downarrow - \varepsilon_s\sigma\overline{T}_{s_0}^4}_{\overline{R}_n} + \underbrace{(1 - \alpha_s)\Delta S_\downarrow(t) + \Delta L_\downarrow(t) - 4\varepsilon_s\sigma\overline{T}_{s_0}^3\Delta T_{s_0}(t)}_{\Delta R_n}, \tag{11}$$

where $\overline{X}$ represents the mean value of X over period T and $\Delta X(t)$ represents the temporal variations of X around its mean.

iv) Entrainment is added on top of the ABL. We introduce a parameter α such that $H(z_i) = -\alpha H(h)$, in order to account for the entrainment of warmer air into the ABL from the free troposphere. In addition, the entrainment of dry air is also represented on top of the ABL with $\lambda E(z_i) = \xi H(z_i)$ $(\lambda \Delta q / C_p \Delta\theta)H(z_i)$, where $\Delta\theta$ is the potential temperature jump and Δq is the specific humidity jump on top of the boundary layer (see Margulis and Entekhabi 2004). This jump ratio is assumed to be constant throughout the day to study the first-order effects of entrainment.

After linearization, the model can be solved in the temporal Fourier domain as in Gentine et al. (2010) that yields both the steady-state and harmonic response of the variables. In particular, the amplitude and phase of all harmonics can be derived as a function of the land surface parameters (vegetation height, soil diffusivity,

TABLE 1. RMSE of surface turbulent heat fluxes from days 100 to 110.

Day	100	101	102	103	104	105	106	107	108	109
RMSE H (W m^{-2})	22.1	27.9	23.9	26.5	16.7	25.1	24.3	26.7	26.9	29.7
RMSE λE (W m^{-2})	26.1	34.9	55.1	45.2	39.7	42.5	69.1	34.3	48.2	48.8

etc.) as well as meteorological conditions (friction velocity, relative humidity, incident surface radiation, etc.).

b. Fourier development

The flux as well as state profiles (soil temperature, ABL potential temperature, and ABL-specific humidity) are assumed to be periodic over the period T so that the different variables can be expanded using Fourier basis functions. Any variable $A(t, z)$ is then developed as a weighted sum of harmonics:

$$A(t,z) = \overline{A}(z) + \sum_{\substack{n=-\infty \\ n\neq 0}}^{n=+\infty} \tilde{A}(n\omega_0, z) e^{jn\omega_0 t}, \qquad (12)$$

with fundamental angular frequency $\omega_0 = 2\pi/T$. By projecting on the Fourier basis, the problem can be solved componentwise—that is, each complex amplitude $\tilde{A}(n\omega_0, z)$ is solved independently from the others and responds to the harmonic forcing of incoming radiation at angular frequency $\omega_n = n\omega_0$: $\tilde{I}_{\downarrow}(\omega_n)$.

The specification of the time series of incoming radiation $I_{\downarrow}(t_k)$ (defined as net solar radiation plus longwave incoming radiation) is sufficient to solve the entire harmonic problem using the assumed temporal periodicity of the solution. In addition to the mean incoming radiation, the steady-state solution requires the knowledge of the mean potential temperature $\overline{\theta}(z_1)$ and specific humidity $\overline{q}(z_1)$ at one given height. We constrain these to be the observed meteorological values at screen-level $z_1 = 2$ m.

The turbulent heat fluxes obtained by the analytical model were compared to in situ measurements for days 100 to 110 (corresponding to Fig. 1) and days 131 to 140 (corresponding to Fig. 2). The root-mean-square error (RMSE) and coefficient of determination R^2 are presented in Tables 1 and 2. There is relatively good agreement between the analytical model and the in situ measurements, especially considering the simplicity of the model and the linearization assumption. During the senescence period (days 131 to 140), the linearization of the surface temperature is less valid because of the large temperature amplitude induced by water limitation. The RMSE is reasonable given the simple construct of the model, further confirming that the daily fluctuations of the turbulent heat fluxes are well captured and reproduced by the land–vegetation–atmosphere model.

c. EF reconstruction in clear-sky conditions

In the SUDMED dataset, 5 continuous days of intensive measurements from 1 to 5 March were selected because the flux measurements were gap free under clear skies. Furthermore, the synoptic conditions over this 5-day period were similar, consistent with the periodicity constraints of the model.

The theoretical coupled land surface and boundary layer model developed in this study is forced with the incident radiation observed during this 5-day period in Fig. 6. The model is assumed to be periodic over the 5-day period T. The root-zone soil water content did not change appreciably during this period and the synoptic conditions were similar during the duration. Figure 7 shows the net radiation and surface ground heat flux comparisons between the model and observations. Figure 8 extends the comparison to the two turbulent heat fluxes. The simple linearized model effectively captures the diurnal course of the surface energy balance components in terms of relative partitioning and dynamic pattern. Figure 9 shows that the linearized model is also able to represent well both soil surface temperature and potential temperature at the height of reference $z_1 = 2$ m. The diurnal course of the two temperatures is realistic and could be used as the lower boundary condition for the ABL domain. Finally, the diurnal course of daytime evaporative fraction is very well captured by the linearized model as shown in Fig. 10.

d. EF minimum–analytical derivation

More insights into the diurnal shape of EF may be gained by deriving the limiting expression for EF. Evaporative fraction is commonly written as

TABLE 2. RMSE of surface turbulent heat fluxes from days 131 to 140.

Day	131	132	133	134	135	136	137	138	139
RMSE H (W m^{-2})	34.2	21.7	29.4	46.4	57.8	33.0	39.5	39.1	58.9
RMSE λE (W m^{-2})	39.0	17.7	25.8	40.7	38.6	25.5	38.6	34.1	29.3

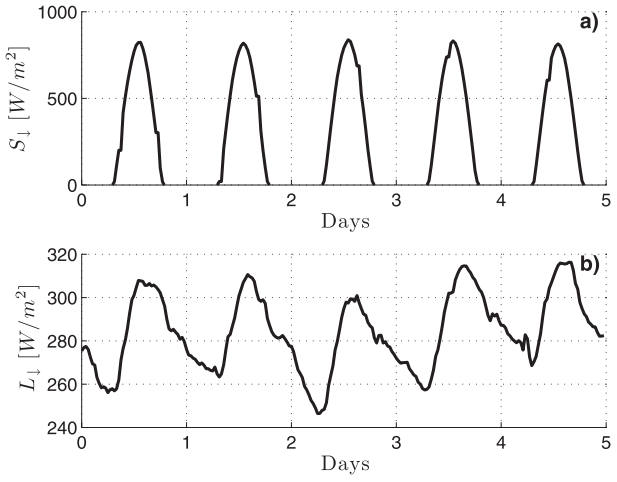

FIG. 6. Sample forcing of (a) shortwave incoming radiation and (b) incoming longwave radiation at the land surface spanning the 1–6 Mar intensive observing period in 2003. The SUDMED experiment covered 101 days and was located near Marrakech, Morocco.

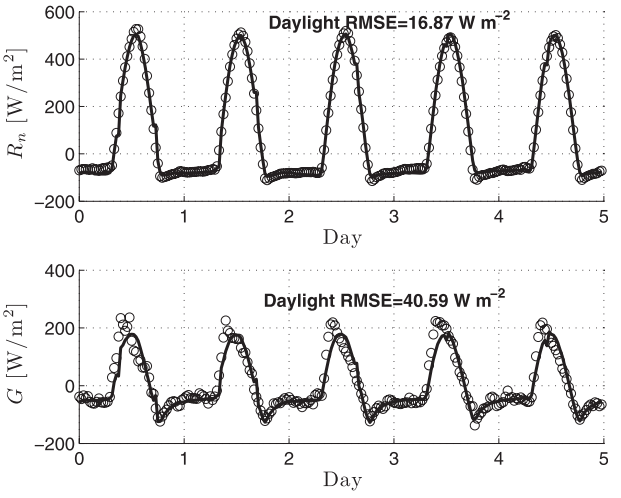

FIG. 7. Comparison of (top) net radiation and (bottom) soil heat flux at the surface for field observations (circles) and the model in this study (lines) from 1 to 6 Mar 2003 using reference values of surface parameters shown in appendix A.

$$\mathrm{EF} = \frac{1}{1 + \dfrac{C_p}{\lambda\beta}\dfrac{T_{s_0} - \theta_h}{q^*(T_{s_0}) - q_h}}, \tag{13}$$

using bulk parameterizations for the turbulent heat fluxes. The term in the denominator is the Bowen ratio. This expression shows that EF mostly removes the effects of turbulence and isolates surface controls, as stated in Gentine et al. (2007). EF is a complex function of soil water availability through β, surface temperature deficit $T_{s_0} - \theta_h$, and water vapor deficit $q^*(T_{s_0}) - q_h$.

The diurnal shape of EF can be diagnosed using (13) and the spectral diagnostic response obtained with the linearized model, namely the daily course of the surface temperature and specific humidity deficits, $T_{s_0} - \theta_h$ and $q^*(T_{s_0}) - q_h$. The deficits in temperature and humidity at the surface are decomposed into steady-state terms (δT_0 and δq_0) that are mostly a function of climate and harmonic terms [$\delta T(t)$ and $\delta q(t)$] that are mostly a function of incident radiation periodicity. The temperature and water vapor deficit at the land surface respond similarly to a forcing of incoming radiation at the land surface (not shown). These results are obtained from the model states and they are used to give insights into the magnitude and phase of the difference quantities—$T_{s_0} - \theta_h$ and $q^*(T_{s_0}) - q_h$—at different harmonics. Taking a well-watered surface condition ($\beta = 0.7$), the ratio of the amplitude remains relatively constant over the whole spectrum (not shown). In addition, the harmonic differences are in phase (not shown). The harmonic responses of $\delta T(t)$ and $\delta q(t)$ are mostly proportional at all frequencies.

Consequently, the temporal responses induced by solar radiative heating can be simplified as

$$\delta q(t) = \sum_{\substack{n=-\infty \\ n\neq 0}}^{+\infty} \widetilde{\delta q}_n \cos(n\omega_0 t + \varphi_n)$$

$$= \Gamma_{\overline{T_{s_0}}} \sum_{\substack{n=-\infty \\ n\neq 0}}^{+\infty} \widetilde{\delta T}_n \cos(n\omega_0 t + \varphi_n) = \Gamma_{\overline{T_{s_0}}} \delta T(t), \tag{14}$$

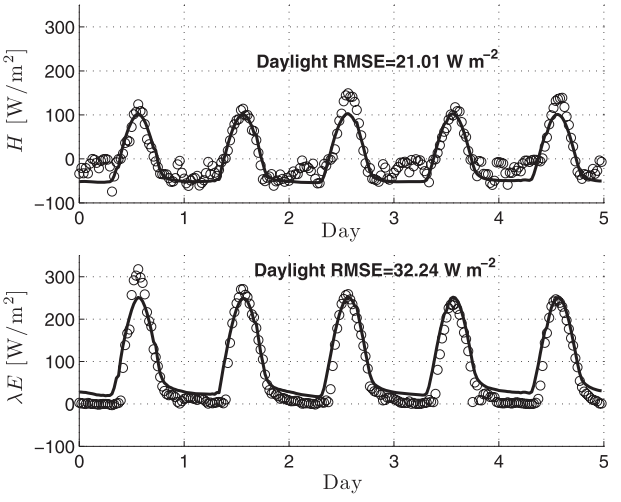

FIG. 8. As in Fig. 7, but for (top) sensible heat flux and (bottom) latent heat flux.

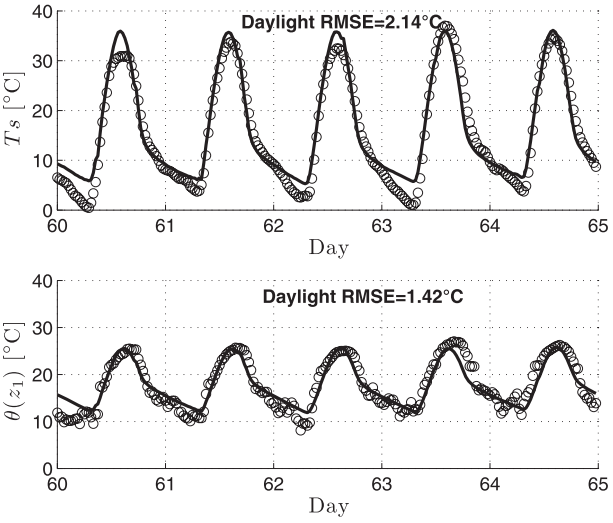

FIG. 9. As in Fig. 7, but for (top) land surface temperature and (bottom) air potential temperature at 2 m.

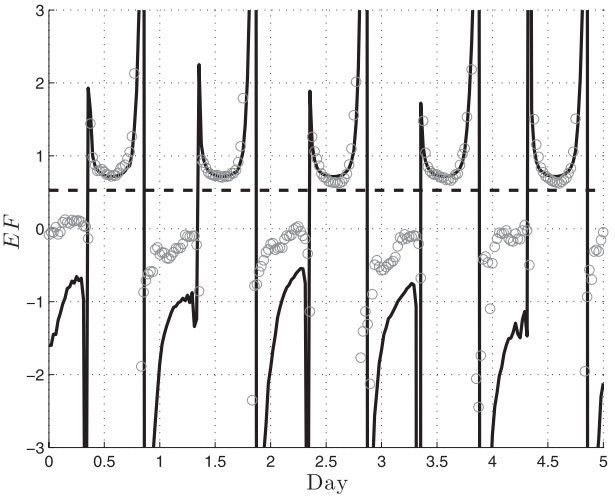

FIG. 10. The EF diurnal cycle (solid line) obtained from soil–vegetation–atmospheric boundary layer continuum model compared to field observations (circles). The theoretical minimum value EF_{min} from (17) is shown as a dashed line.

with

$$\Gamma_{\overline{T_{s_0}}} \approx \gamma_{\overline{T_{s_0}}} \left| \frac{2K_* r_a^c - j\rho\pi - 2\rho \ln(x_h/2) - 2\rho\gamma}{2K_* r_a^c - \beta(j\rho\pi + 2\rho \ln(x_h/2) + 2\rho\gamma)} \right| \in \mathbb{R}^+, \tag{15}$$

where $\gamma_{\overline{T_{s_0}}}$ is the slope of the saturation-specific humidity at the mean land surface temperature $\overline{T_{s_0}}$ and $x_h = 2\sqrt{-[j\omega_0(h-d)/K_*]}$ (see detailed derivation in appendix B). In most cases, $\Gamma_{\overline{T_{s_0}}} \approx \gamma_{\overline{T_{s_0}}}$.

EF is then rewritten as

$$\mathrm{EF} \approx \frac{1}{1 + \dfrac{C_p}{\lambda\beta} \dfrac{\delta T_0 + \delta T(t)}{\delta q_0 + \Gamma_{\overline{T}_{s_0}} \delta T(t)}} = \frac{1}{1 + \dfrac{C_p}{\lambda\beta} \dfrac{\delta T_0 + \delta T(t)}{\delta q_0 + \gamma_{\overline{T}_{s_0}} \delta T(t)}}. \tag{16}$$

When $|\delta T(t)| \gg \max(|\delta T_0|, |\delta q_0|/\gamma_{\overline{T}_{s_0}})$ (condition I), EF tends to its asymptotical value:

$$\mathrm{EF}_{\min} = \frac{1}{1 + \dfrac{1}{\Gamma_{\overline{T_{s_0}}}} \dfrac{C_p}{\lambda\beta}} \approx \frac{1}{1 + \dfrac{1}{\gamma_{\overline{T_{s_0}}}} \dfrac{C_p}{\lambda\beta}}, \tag{17}$$

which corresponds to the observed constant value of evaporative fraction. This condition is approached around solar noon as shown in Fig. 10 with the SUDMED data. Indeed, at noon under strong solar heating, the temperature difference reaches a maximum value and the temperature deficit $\delta T(t)$ becomes large compared to the other parameters. Thus, EF reaches its asymptotical minimum value.

Therefore, in fair-weather conditions with strong solar radiative forcing, EF rapidly approaches its asymptotic value EF_{min} during most of the day. The specific humidity deficit also plays a strong role on EF. In humid regions, evaporation is not limited by the surface soil and vegetation but is instead limited by atmospheric aridity and available energy. The limiting condition defined for EF cannot be reached in very arid regions (see the subsection on dependency on specific humidity deficit) since $T_{s_0} - \theta_h$ is not large enough to compensate for the atmospheric aridity. The importance of these factors is further discussed in the next section.

The power spectrum of incident radiation has a fundamental impact on the EF spectrum and on its diurnal behavior. Indeed, any high order harmonic of incident radiation will strongly influence EF. In the SUDMED dataset used in this study, the main harmonic actually corresponds to the principal daily harmonic $\omega_0 = 2\pi/T_{\mathrm{day}}$. The second daily harmonic also reaches its maximum around noon and contributes to the asymptotic behavior of EF at that time. The effect of the other harmonics on EF is negligible. This behavior is due to the fact that the influence of the first daily harmonic is almost sufficient to explain the diurnal shape of EF, as demonstrated with the sinusoidal reconstruction. However, any noticeable changes in the power spectrum of solar incoming radiation, such as those induced by clouds, will strongly modify the diurnal shape of EF, leading to an erratic aspect with important high-frequency harmonics (see Fig. 1 and Fig. 2).

e. Dependence on environmental factors

In this section, we investigate the dependence of the phase and amplitude of the main daily harmonic of turbulent heat fluxes at $T = 24$ h. Understanding these

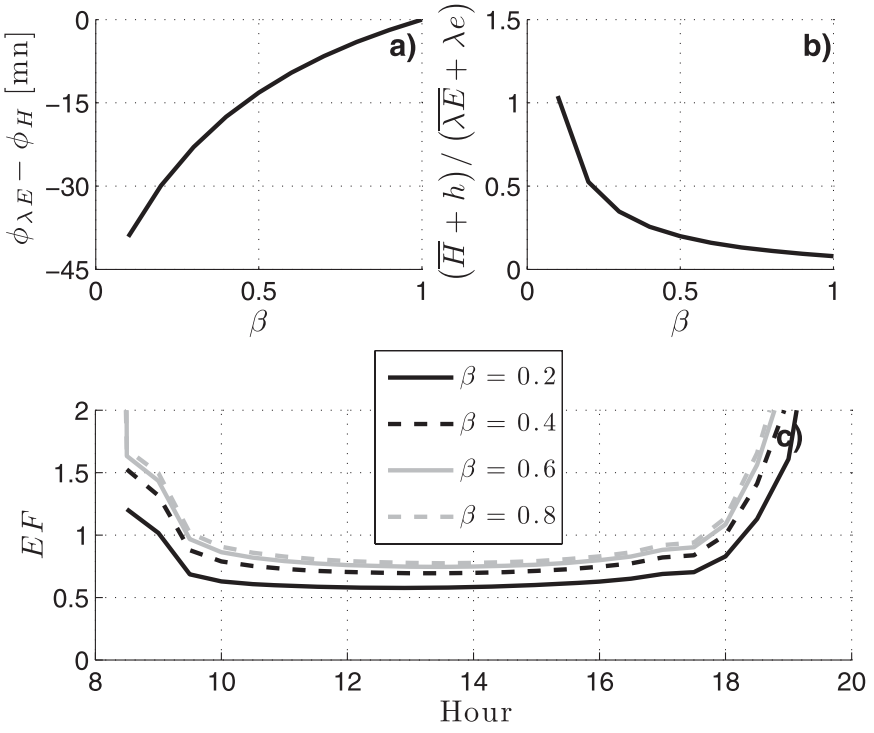

FIG. 11. a) Phase difference between latent heat and sensible heat flux as a function of water availability. b) Amplitude ratio of sensible heat to latent heat flux as a function of water availability. c) Evaporative fraction as a function of hour of day for water availability from 0.2 to 0.8. Phase is expressed in minutes.

dependencies on physical factors in the environment is the pathway through which the degree of self preservation in EF and the convexity of EF during daytime are isolated and diagnosed.

1) DEPENDENCE ON WATER AVAILABILITY β

Clearly, water availability increases EF (see Lhomme and Elguero 1999; Gentine et al. 2007), yet its effect on the diurnal shape of EF is less clear. As shown in Fig. 11, at low water availability latent heat flux lags sensible heat flux by about 40 min, whereas both fluxes are almost in phase when water is not limiting. This signifies that there is an increased inertia in the latent heat response at low water content compared to the sensible heat flux response. The ratio of the amplitude of sensible to latent heat flux $(\overline{H}+h)/(\overline{\lambda E}+\lambda e)$ [h and λe being the amplitude of the daily ($T = 24$ h) principal harmonic of sensible and latent heat flux] depicted in Fig. 11b shows that this ratio goes from about 1 at low water availability ($\beta = 0.2$) to 0.1 at very high water contents ($\beta = 0.8$). Consequently, when water is not limiting and the skies are cloud free, EF takes on a typical convex U shape with a noticeable symmetry (induced by the reduced phase difference). When water is limiting and the ratio $(\overline{H}+h)/(\overline{\lambda E}+\lambda e)$ has increased so much that the effect of the phase is small, a distinct asymmetry in the daytime pattern of EF develops. This asymmetry is characterized by enhanced rise in late afternoon and it is often observed in evaluations of EF using field observations.

2) DEPENDENCE ON SOLAR INCOMING RADIATION

The influence of the magnitude of solar radiation is significant and shown in Fig. 12. Solar radiation does not have any direct effect on the phase difference between sensible and latent heats for the linear model. However, the magnitude of solar radiation has an important effect on the energy partitioning between sensible and latent heat fluxes $(\overline{H}+h)/(\overline{\lambda E}+\lambda e)$ as seen in Fig. 12. The ratio $(\overline{H}+h)/(\overline{\lambda E}+\lambda e)$ increases with increasing solar radiation. When the solar radiation is high, evaporation becomes water limited, whereas it is an energy-limited regime at lower values of solar radiation. The solar radiation factor modifies in a subtle way both the daily mean and the principal harmonic response of sensible and latent heat fluxes.

The self-preservation of EF appears more clearly at high values of solar incoming radiation. Under these conditions, EF reaches its asymptotic value EF_{min}

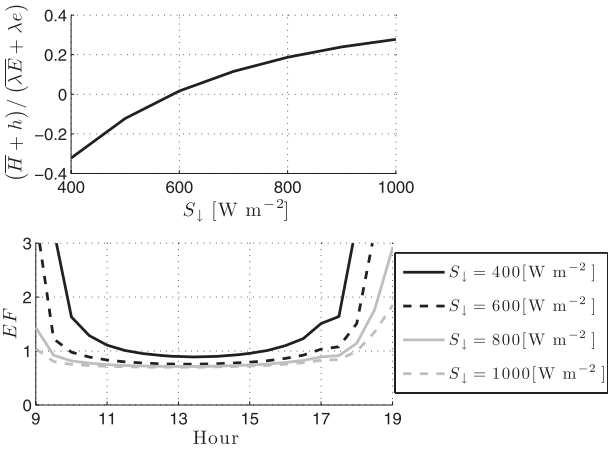

FIG. 12. (bottom) Diurnal course of EF for maximum diurnal values of shortwave incoming radiation of 200, 400, 600, or 800 (W m^{-2}), along with (top) the ratio of the mean-daily and first harmonic of sensible to that of latent heat flux.

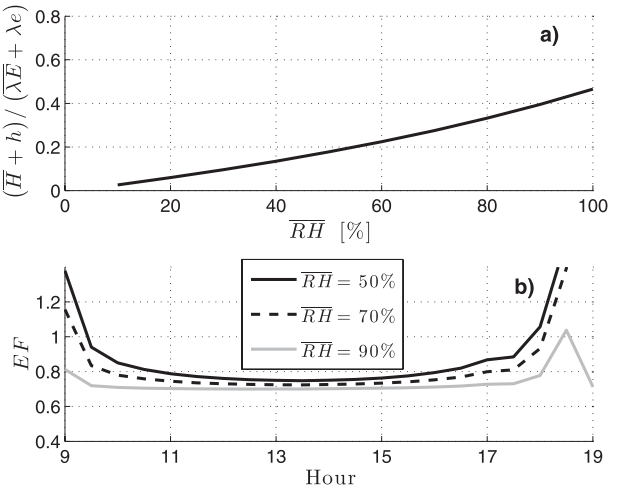

FIG. 13. a) Ratio of sensible to latent heat flux as a function of relative humidity. b) Diurnal course of EF as a function of hour of the day for relative humidity from 50% to 90%.

earlier in the day. EF reaches its asymptotical value only when solar radiation is appreciable. High values of solar radiation induce an important temperature gradient (approaching condition I; see section 4d) at the land surface. The diurnal course of evaporative fraction in cloudy and intermittent-cloudy conditions depends on the degree of attenuation and the duration of coverage.

3) Dependence on friction velocity

Friction velocity does not impact the midday value of EF (not shown) but does impact its daytime shape. At low values of friction velocity, EF is nearly constant, yet there is a noticeable tendency toward a convex U shape at high-friction velocities. Two simultaneous effects can be the cause of these results. First, the impact of friction velocity on the phase difference between sensible and latent heat flux is negligible. It, however, modifies the ratio $(\overline{H}+h)/(\overline{\lambda E}+\lambda e)$, inducing a more pronounced U shape at higher values of friction velocity (not shown). This is similar to the simple sinusoidal analog of EF presented in section 4. Second, the expression of the asymptotical value of EF is not explicitly dependent on friction velocity. Therefore, the minimum value is similar across a wide range of friction velocities. This confirms the conclusion of Lhomme and Elguero (1999) but gives theoretical underpinning to this lack of sensitivity.

4) Dependence on relative humidity

Figure 13 shows the sensitivity of EF to the daily-mean relative humidity deficit. Daily-mean relative humidity is mostly a function of passing synoptic-scale weather systems and mean-daily solar radiation. The subdiurnal fluctuations around this daily-mean value or spectral amplitudes are instead mostly related to the magnitude of radiation forcing. The mean relative humidity does not affect the phase between latent and sensible heat fluxes, but it does modify the energy partitioning $(\overline{H}+h)/(\overline{\lambda E}+\lambda e)$. The effect is to introduce a pronounced concavity or U shape to EF at low daily-mean relative humidity.

The diurnal course of EF remains fairly constant only for the highest values of mean relative humidity (75%–90%). When the air is dry (<50%), the diurnal course of EF is noticeably parabolic. Consequently, the use of a constant EF during daytime should be more applicable over humid rather than semiarid regions. The sensitivity of EF to the mean relative humidity can also be explained by condition I: solar radiation has to be sufficient to create a land surface temperature gradient that will counteract the mean specific humidity deficit and the atmospheric aridity. This is also confirmed by the fact that the Bowen ratio, which appears in the denominator of EF, decreases when the air is more humid.

5) Dependence on boundary layer entrainment

The effect of a change in the entrainment on top of the ABL is investigated in Fig. 14 by modifying the parameter α, which controls the rate of warm and dry air entrainment at the ABL top. This and the Bowen ratio at the top of the ABL exhibit intraday variability as shown in Stull (1988), Peters-Lidard and Davis (2000), Margulis and Entekhabi (2004), and Santanello et al. (2005). Here we use constant parameters in order to

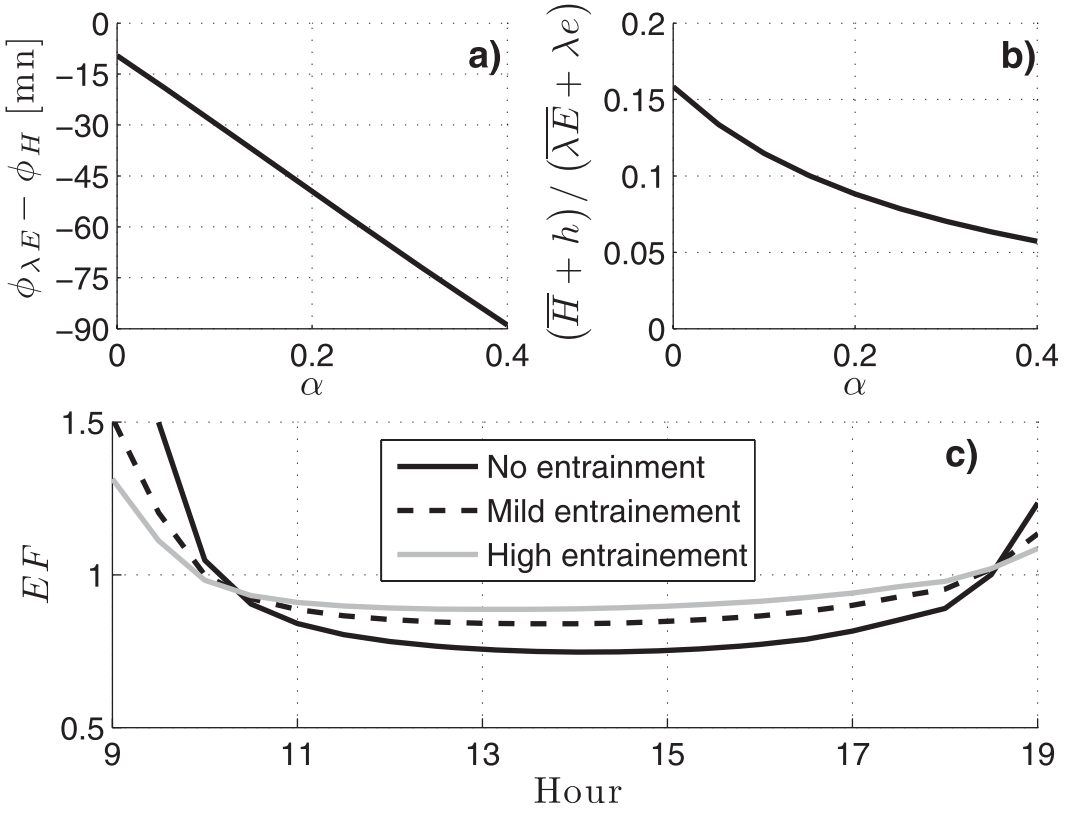

FIG. 14. a) Phase difference between latent heat and sensible heat flux as a function of entrainment rate. b) Amplitude ratio of sensible heat to latent heat flux as a function of entrainment rate. (c) Diurnal course of EF as a function of the entrainment on top of the ABL (no-entrainment case corresponds to $\alpha = 0$ and $\xi = 0$, mild entrainment to $\alpha = 0.2$ and $\xi = 0.5$, and strong entrainment to $\alpha = 0.4$ and $\xi = 2$). Phase is expressed in minutes.

study the first-order impact of the entrainment on EF. The value of α is commonly reported to be between 0.2 and 0.4. Typical values of the parameter of entrainment of dry air on top of the ABL are of the order of 0.5 to 5 times that of potential temperature. We use three main sets of parameters: no-entrainment case with $\alpha = 0$ and $\xi = 0$, mild entrainment $\alpha = 0.2$ and $\xi = 0.5$, and strong entrainment $\alpha = 0.4$ and $\xi = 2$.

Figure 14a shows that the main effect of the boundary layer entrainment is to modify the phase between sensible and latent heat flux. This is also accompanied by a reduction of the ratio between sensible and latent heat flux. This effect is due to the fact that during daylight hours the entrainment of dry and warm air from above simultaneously increases latent heat flux and decreases sensible heat flux at the surface through the modification of the near-surface air humidity and temperature. The air temperature in the boundary layer is increased with the entrainment of warmer air from above. This is due to the sensible heat on top of the ABL. This consequently reduces the temperature gradient at the surface. Similarly, the entrainment of dry air from above the ABL reduces the specific humidity in the ABL, thus raising the specific humidity gradient at the land surface and enhancing the surface latent heat flux. Consequently, the effect of strong entrainment is to reduce the concave or U shape of EF and to induce stronger self-preservation. In addition, the midday value of EF is increased with the enhanced entrainment as shown in Fig. 14c.

5. Conclusions

This study investigates the physical factors and underlying causes for the breakdown of daytime preservation of evaporative fraction. Based on long duration (>70 days) of field observations, we show that evaporative fraction is seldom constant during daytime. It is mostly characterized by broad (temporal) spectrum, whereas sensible and latent heat fluxes have most of the spectral energy at the daily and semidiurnal frequencies. Evaporative fraction as a ratio of these fluxes (ratio of

latent heat flux to sum of latent and sensible heat fluxes) is, in the frequency domain, a convolution of the sensible and latent heat fluxes. Hence, even though the turbulent heat fluxes may be simple periodic functions, any phase difference between them or any perturbations such as those introduced by intermittent cloudiness will result in a broad spectrum for EF. In time domain, we use a simple sinusoidal analog for both latent and sensible heat fluxes and show that any phase difference between the two or any offset in their mean values or daily amplitudes will result in the typically observed concave (often asymmetric) EF pattern.

The phase difference and amplitude ratios are key determinants of the daytime shape of EF. We focus on these two variables and introduce a model that can isolate the influence of physical and environmental factors on them. The phase and gain spectra of the profiles and fluxes in a soil–vegetation–atmospheric boundary layer continuum are derived. To express the states and fluxes in terms of Fourier basis functions, the model has to be linear. We extend the linear coupled soil–atmosphere model of Gentine et al. (2010) and Lettau (1951) to apply to this study. The addition of a dynamic evaporation model, introduction of a vegetation layer, and solution across all harmonics are the main enhancements that are needed.

The phase and amplitude dependency of the principal harmonic ($T = 24$ h) of the turbulent heat fluxes is investigated with the model. Evaporative fraction decreases with the mean-daily relative humidity and solar radiation. Daytime self-preservation is mainly confined to high values of relative humidity and solar radiation. For lower values of solar incoming radiation, EF exhibits a strongly parabolic and convex pattern during daytime (limited to fair-weather and clear-sky conditions). Evaporative fraction is not sensitive to the values of friction velocity. The daytime pattern of evaporative fraction is, however, sensitive to entrainment of warm and dry air from above the ABL. Increased entrainment raises the daylight evaporative fraction. Evaporative fraction exhibits daytime self-preservation only under the limited conditions of clear skies, humid air, and strong solar radiation.

In this study, we derived the minimum asymptotical value (17) of evaporative fraction based on the analytical model. This asymptotic value applies at midday when the magnitude of latent and sensible heat flux are highest and the knowledge of evaporative fraction is the most relevant.

Acknowledgments. This work was carried out with support from the grant titled ''Direct Assimilation of Remotely Sensed and Surface Temperature for the estimation of Surface Fluxes'' from the National Aeronautics and Space Administration to Massachusetts Institute of Technology. The authors thank the SUDMED project team for providing the experimental dataset from the region of Marrakech, Morocco. We thank three anonymous reviewers for their important comments, which have helped improve the manuscript.

APPENDIX A

List of Variables and Units

$\overline{X}$	Mean (steady-state) value of variable X
$\tilde{X}(\omega_n)$	Harmonic (Fourier transform) of variable X at frequency ω_n
α_s	Albedo of the land surface (0.16)
α	Potential temperature entrainment on top of the boundary layer: $H(z_i)/H(h)$
β	Beta factor in the Deardorff (1978) parameterization of latent heat flux at the land surface (0.6 dimensionless)
γ	Euler's constant
γ_T	Partial derivative of saturation-specific humidity with respect to temperature taken at temperature T (kg kg^{-1} K^{-1})
λ	Specific latent heat of vaporization
λE_h	Latent heat flux at the land surface at canopy height h (W m^{-2})
ω	Angular frequency of the harmonic (rad s^{-1})
ω_0	Fundamental harmonic $2\pi/T$ (rad s^{-1})
ρ	Density of air
θ	Potential temperature (K)
θ_h	Potential temperature at vegetation height h (K)
ξ	Specific humidity entrainment parameter on top of the boundary layer: $\lambda E(z_i)/\lambda E(h)$
A	Available energy at the land surface (W m^{-2})
C_s	Soil heat capacity (1.42×10^6 J m^{-3} K^{-1})
EF	Evaporative fraction at the land surface (dimensionless)
G_0	Ground heat flux at the land surface (W m^{-2})
H	Vegetation height (0.45 m)
H_h	Sensible heat flux at the land surface right above the canopy (W m^{-2})
K_*	Product of Von Kármán constant and friction velocity $K_* = Ku_*$
K_s	Soil thermal diffusivity (2.5×10^{-7} m^2 s^{-1})
$L_\downarrow$	Shortwave incoming radiation at the land surface (W m^{-2})
LAI	Leaf area index (0.4 m^2 m^2)
Q	Specific humidity (kg kg^{-1})
q_a	Specific humidity at screen level (kg kg^{-1})
q_h	Specific humidity at vegetation height h (kg kg^{-1})

q^* Specific humidity at saturation (kg kg^{-1})
r_a^c Canopy aerodynamic resistance between canopy and within canopy source height (50 s m^{-1})
R_n Net radiation at the land surface (W m^{-2})
$S_\downarrow$ Shortwave incoming radiation at the land surface (W m^{-2})
T Time period (24 h)
T_a Air temperature at screen level (K)
T_s Soil temperature (K)
T_{s_0} Land surface temperature $T_{s_0} = T_s(0)$ (K)
T_{day} Duration of a day
u_* Friction velocity (0.1 m s^{-1})
z Height in ABL and depth in soil (m)
z_1 Screen height (2 m)
z_i Height of the boundary layer

APPENDIX B

Derivation of Minimum Daylight Evaporative Fraction

The net radiation at the surface is linearized around the mean land surface temperature:

$$R_n(t) = \underbrace{\overline{I}_\downarrow - \varepsilon_s \sigma \overline{T}_{s_0}^4}_{\overline{R}_n} + \underbrace{\sum_{\substack{k=-\infty \\ k\neq 0}}^{\infty} [\widetilde{I_\downarrow}(\omega_k) - 4\varepsilon_s \sigma \overline{T}_{s_0}^3 \widetilde{T_{s_0}}(\omega_k)] e^{j\omega_k t}}_{\delta R_n(t)}, \tag{B1}$$

where $I_\downarrow = (1 - \alpha_s)S_\downarrow + L_\downarrow$ is the incoming radiation minus the outgoing solar radiation from the surface, $\overline{T_{s_0}}$ is the mean land surface temperature over the period of interest (five days in this experiment).

Using a similar derivation to the one introduced by Gentine et al. (2010), it can be shown that the complex amplitude of sensible heat flux at the surface can be written as

$$\widetilde{H_h}(\omega_n) = \frac{\rho C_p \Delta(\omega_n)}{[r_a^c + \rho\Sigma(\omega_n)]\left\{1 + 4\varepsilon_s \sigma \overline{T}_{s_0}^3 \Delta(\omega_n) + \rho\Delta(\omega_n)\left[\dfrac{C_p}{r_a^c + \rho\Sigma(\omega_n)} + \dfrac{\lambda\beta\gamma_{\overline{T}_{s_0}}}{r_a^c + \rho\beta\Sigma(\omega_n)}\right]\right\}} \widetilde{I}_\downarrow(\omega_n), \tag{B2}$$

and the latent heat flux can be written as

$$\widetilde{\lambda E_h}(\omega_n) = \frac{\lambda\beta\gamma_{\overline{T}_{s_0}} \Delta(\omega_n)}{[r_a^c + \rho\beta\Sigma(\omega_n)]\left\{1 + 4\varepsilon_s \sigma \overline{T}_{s_0}^3 \Delta(\omega_n) + \rho\Delta(\omega_n)\left[\dfrac{C_p}{r_a^c + \rho\Sigma(\omega_n)} + \dfrac{\lambda\beta\gamma_{\overline{T}_{s_0}}}{r_a^c + \rho\beta\Sigma(\omega_n)}\right]\right\}} I_\downarrow e^{j\alpha}(\omega_n), \tag{B3}$$

where $\widetilde{I}_\downarrow(\omega_n)$ is the complex amplitude of $I_\downarrow(t)$ at frequency ω_n,

$$\Delta(\omega_n) = \frac{1}{C_s}(1 - j)\sqrt{\frac{1}{2\omega_n K_s}}, \tag{B4}$$

and

$$\Sigma(\omega_n) = \frac{1}{K_* x_h} \frac{H_1^1(x_i)H_0^2(x_h) - H_1^2(x_i)H_0^1(x_h)}{H_1^1(x_i)H_1^2(x_h) - H_1^2(x_i)H_1^1(x_h)}, \tag{B5}$$

with $x_h = 2\sqrt{-j\omega_n(h-d)/K_*}$ and H_1^1 denoting the Hankel function of the first order and first kind, representing an inward wave for the z coordinate, and H_1^2 is the Hankel function of the first order and second kind, which represents an outward wave.

Now the Fourier decomposition of $q^*(T_{s_0}) - q_h$ and $T_{s_0} - \theta_h$ can be derived from (B2) and (B3) together with the bulk definition of latent heat flux (9) and sensible heat flux $H_h = \rho C_p(T_{s_0} - \theta_h)/r_a^c$. The ratio of the complex amplitude of the deficit of specific humidity $\widetilde{\delta q}(\omega_n) \triangleq \widetilde{q^*(T_{s_0}) - q_h}(\omega_n)$ to that of temperature at the surface $\widetilde{\delta T}(\omega_n) \triangleq \widetilde{T_{s_0} - \theta_h}(\omega_n)$ can then be rewritten and expanded in series form using (B2) and (B3) as

$$\Gamma_{\overline{T_{s_0}}} = \frac{\widetilde{\delta q}(\omega_n)}{\widetilde{\delta T}(\omega_n)} = \gamma_{\overline{T_{s_0}}} \frac{1 + \dfrac{\rho\Sigma(\omega_n)}{r_a^c}}{1 + \beta\dfrac{\rho\Sigma(\omega_n)}{r_a^c}}$$

$$\approx \gamma_{\overline{T_{s_0}}} \left| \frac{2K_* r_a^c - j\rho\pi - 2\rho\ln(x_h/2) - 2\rho\gamma}{2K_* r_a^c - \beta(j\rho\pi + 2\rho\ln(x_h/2) + 2\rho\gamma)} \right|. \quad \text{(B6)}$$

Under most conditions $|H_1^2(x_i)| \ll |H_1^1(x_i)|$ by at least two orders of magnitude as long as entrainment is moderate. This value is not frequency dependent so that the approximation can be evaluated at the principal harmonic ω_0. It should be also noted that the value is real and positive since the phase difference between the specific humidity deficit and that of temperature is almost zero. In most cases, the term in the absolute value is close to one and $\Gamma_{\overline{T_{s_0}}} \approx \gamma_{\overline{T_{s_0}}}$.

REFERENCES

Boni, G., F. Castelli, and D. Entekhabi, 2001a: Sampling strategies and assimilation of ground temperature for the estimation of surface energy balance components. *IEEE Trans. Geosci. Remote Sens.,* **39,** 165–172.

——, D. Entekhabi, and F. Castelli, 2001b: Land data assimilation with satellite measurements for the estimation of surface energy balance components and surface control on evaporation. *Water Resour. Res.,* **37,** 1713–1722.

Brubaker, K. L., and D. Entekhabi, 1994: Nonlinear dynamics of water and energy balance in land-atmosphere interaction. Ralph M. Parsons Lab. Tech. Rep. 341, Massachusetts Institute of Technology, 166 pp.

Caparrini, F., F. Castelli, and D. Entekhabi, 2003: Mapping of land-atmosphere heat fluxes and surface parameters with remote sensing data. *Bound.-Layer Meteor.,* **107,** 605–633.

——, ——, and ——, 2004a: Estimation of surface turbulent fluxes through assimilation of radiometric surface temperature sequences. *J. Hydrometeor.,* **5,** 145–159.

——, ——, and ——, 2004b: Variational estimation of soil and vegetation turbulent transfer and heat flux parameters from sequences of multisensor imagery. *Water Resour. Res.,* **40,** W12515, doi:10.1029/2004WR003358.

Chehbouni, A., and Coauthors, 2008: An integrated modelling and remote sensing approach for hydrological study in arid and semi-arid regions: The SUDMED Program. *Int. J. Remote Sens.,* **29,** 5161–5181.

Crago, R., 1996: Conservation and variability of the evaporative fraction during the daytime. *J. Hydrol.,* **180,** 173–194.

——, and W. Brutsaert, 1996: Daytime evaporation and the self-preservation of the evaporative fraction and the Bowen ratio. *J. Hydrol.,* **178,** 241–255.

Deardorff, J. W., 1978: Efficient prediction of ground surface temperature and moisture, with inclusion of a layer of vegetation. *J. Geophys. Res.,* **83,** 1889–1903.

Duchemin, B., and Coauthors, 2006: Monitoring wheat phenology and irrigation in Central Morocco: On the use of relationships between evapotranspiration, crops coefficients, leaf area index and remotely-sensed vegetation indices. *Agric. Water Manage.,* **79,** 1–27.

Gentine, P., D. Entekhabi, A. Chehbouni, G. Boulet, and B. Duchemin, 2007: Analysis of evaporative fraction diurnal behaviour. *Agric. For. Meteor.,* **143,** 13–29.

——, ——, and J. Polcher, 2010: Spectral behaviour of a coupled land-surface and boundary-layer system. *Bound.-Layer Meteor.,* **134,** 157–180, doi:10.1007/s10546-009-9433-z.

Kim, C. P., and D. Entekhabi, 1998: Feedbacks in the land-surface and mixed-layer energy budgets. *Bound.-Layer Meteor.,* **88,** 1–21.

Kimura, F., and Y. Shimizu, 1994: Estimation of sensible and latent heat fluxes from soil surface temperature using a linear air–land heat transfer model. *J. Appl. Meteor.,* **33,** 477–489.

Kustas, W., T. Jackson, A. French, and J. MacPherson, 2001: Verification of patch- and regional-scale energy balance estimates derived from microwave and optical remote sensing during SGP97. *J. Hydrometeor.,* **2,** 254–273.

Lettau, H., 1951: Theory of surface temperature and heat-transfer oscillations near level ground surface. *Eos, Trans. Amer. Geophys. Union,* **32,** 189–200.

Lhomme, J.-P., and E. Elguero, 1999: Examination of evaporative fraction diurnal behaviour using a soil-vegetation model coupled with a mixed-layer model. *Hydrol. Earth Syst. Sci.,* **3,** 259–270.

Manqian, M., and J. Jinjun, 1993: A coupled model on land-atmosphere interactions—Simulating the characteristics of the PBL over a heterogeneous surface. *Bound.-Layer Meteor.,* **66,** 247–264.

Margulis, S. A., and D. Entekhabi, 1998: Temporal disaggregation of satellite derived monthly precipitation estimates for use in hydrological applications. Massachusetts Institute of Technology, Department of Civil Engineering Tech. Rep. 344, 98 pp.

——, and ——, 2004: Boundary-layer entrainment estimation through assimilation of radiosonde and micrometeorological data into a mixed-layer model. *Bound.-Layer Meteor.,* **110,** 405–433.

——, D. McLaughlin, D. Entekhabi, and S. Dunne, 2002: Land data assimilation and estimation of soil moisture using measurements from the Southern Great Plains 1997 Field Experiment. *Water Resour. Res.,* **38,** 1299, doi:10.1029/2001WR001114.

Nichols, W. E., and R. H. Cuenca, 1993: Evaluation of the evaporative fraction for parameterization of the surface energy balance. *Water Resour. Res.,* **29,** 3681–3690.

Peters-Lidard, C. D., and L. H. Davis, 2000: Regional flux estimation in a convective boundary layer using a conservation approach. *J. Hydrometeor.,* **1,** 170–182.

Santanello, J. A., M. A. Friedl, and W. P. Kustas, 2005: An empirical investigation of convective boundary layer evolution and its relationship with the land surface. *J. Appl. Meteor.,* **44,** 917–932.

Shuttleworth, W. J., R. J. Gurney, A. Y. Hsu, and J. P. Ormsby, 1989: FIFE: The variation in energy partition at surface flux sites. *IAHS Publ.,* **186,** 67–74.

Stull, R. B., 1988: *An Introduction to Boundary Layer Meteorology*. Kluwer Academic Publishers, 666 pp.

Van de Wiel, B. J. H., A. F. Moene, R. J. Ronda, H. A. R. De Bruin, and A. A. M. Holtslag, 2002: Intermittent turbulence and oscillations in the stable boundary layer over land. Part II: A system dynamics approach. *J. Atmos. Sci.,* **59,** 2567–2581.

Wang, Z., and L. A. Mysak, 2000: A simple coupled atmosphere–ocean–sea ice–land surface model for climate and paleoclimate studies. *J. Climate,* **13,** 1150–1172.

Zeng, N., and J. D. Neelin, 1999: A land–atmosphere interaction theory for the tropical deforestation problem. *J. Climate,* **12,** 857–872.